Acta Crystallographica Section F
Structural Biology and Crystallization Communications
ISSN 1744-3091

Crystallization and preliminary X-ray analysis of the inducible lysine decarboxylase from *Escherichia coli*

Eftichia Alexopoulos,[a,b]‡ Usheer Kanjee,[a]‡ Jamie Snider,[a] Walid A. Houry[a]* and Emil F. Pai[a,b,c]*

[a]Department of Biochemistry, University of Toronto, 1 King's College Circle, Medical Sciences Building, Toronto, Ontario M5S 1A8, Canada, [b]Department of Medical Biophysics, University of Toronto, Division of Cancer Genomics and Proteomics, Ontario Cancer Institute, Toronto Medical Discovery Tower, 101 College Street, Toronto, Ontario M5G 1L7, Canada, and [c]Department of Molecular Genetics, University of Toronto, 1 King's College Circle, Medical Sciences Building, Toronto, Ontario M5S 1A8, Canada

‡ These authors contributed equally to this publication.

Correspondence e-mail: walid.houry@utoronto.ca, pai@hera.med.utoronto.ca

Received 12 May 2008
Accepted 20 June 2008

The decameric inducible lysine decarboxylase (LdcI) from *Escherichia coli* has been crystallized in space groups $C2$ and $C222_1$; the $Ta_6Br_{12}^{2+}$ cluster was used to derivatize the $C2$ crystals. The method of single isomorphous replacement with anomalous scattering (SIRAS) as implemented in *SHELXD* was used to solve the $Ta_6Br_{12}^{2+}$-derivatized structure to 5 Å resolution. Many of the $Ta_6Br_{12}^{2+}$-binding sites had twofold and fivefold noncrystallographic symmetry. Taking advantage of this feature, phase modification was performed in *DM*. The electron-density map of LdcI displays many features in agreement with the low-resolution negative-stain electron-density map [Snider *et al.* (2006), *J. Biol. Chem.* **281**, 1532–1546].

1. Introduction

Bacterial cells possess elegant regulatory systems to alleviate stresses under harsh conditions and to take advantage of favourable environments. One of the most frequently encountered hostile conditions is acid stress. Neutralophiles such as *Escherichia coli*, *Salmonella enterica* and *Shigella flexneri* must survive passage through the acidic conditions of the stomach, which has a pH of about 2 with an emptying time of approximately 2 h (Texter *et al.*, 1968; Texter, 1968), before reaching the less acidic environment of the intestinal tract (pH 4.5–7; Gorden & Small, 1993) where pathogenesis occurs. The ability of a bacterium to withstand acid stress has been directly correlated with its infectious dose (Boyd, 1995; Richard & Foster, 2003). Consequences of acid stress include an acidified internal pH followed by damage to various macromolecules. Therefore, bacteria have evolved very complex acid-stress response systems that involve more than 50 acid-shock proteins (Foster, 1993; Lee *et al.*, 1995).

In *E. coli*, a major adaptation to low pH is the induction of a number of amino-acid decarboxylases that are capable of raising the intracellular pH *via* their proton-dependent amino-acid decarboxylation activity (Foster, 2004). Four such systems have been identified that employ the following proteins: the homologous inducible glutamate decarboxylases GadA and GadB, the inducible arginine decarboxylase AdiA, the inducible ornithine decarboxylase SpeF (Iyer *et al.*, 2003; Kashiwagi *et al.*, 1991) and the inducible lysine decarboxylase LdcI (Snider *et al.*, 2006). GadA, GadB and AdiA are involved in survival under extreme acid-stress conditions along with several other nondecarboxylase systems, while SpeF and LdcI are active under milder acid-stress conditions. A common feature among the amino-acid decarboxylases is their use of pyridoxal 5′-phosphate (PLP) as an enzyme cofactor.

LdcI catalyzes the decarboxylation of the α-carboxyl group of L-lysine to form the polyamine cadaverine and carbon dioxide. The reaction consumes a proton, thus serving to raise the intracellular pH during acid-stress conditions. An inner membrane-bound lysine-cadaverine antiporter CadB is also active under acid-stress conditions and acts to resupply LdcI with the substrate lysine and remove the cadaverine generated by the decarboxylation reaction. The genes for

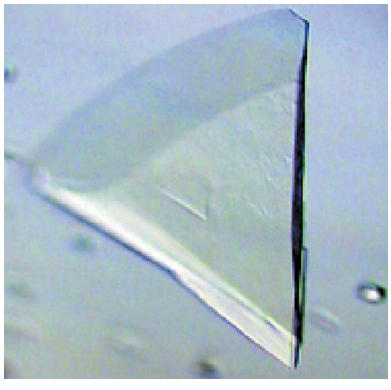

Table 1
Data-collection statistics for *C*2 (Native-1), *C*2 $Ta_6Br_{12}^{2+}$ derivative (Derivative-1) and $C222_1$ (Native-2) crystal forms.

Values in parentheses refer to the highest 0.1 Å resolution shell. X-ray sources refer to the beamlines at the Advanced Photon Source (APS), Argonne National Laboratories (ANL), Chicago, Illinois, USA. Data-set statistics were analyzed using *XPREP* (Bruker, 2000).

Data set	Native-1	Derivative-1	Native-2
X-ray source	SBC-19BM-D	SBC-19BM-D	BioCARS14-BM-C
Wavelength (Å)	1.2544	1.2544	0.9002
Detector	SBC3-CCD	SBC3-CCD	ADSC Quantum 315
Temperature (K)	100	100	100
Space group	*C*2	*C*2	$C222_1$
Unit-cell parameters			
a (Å)	270.4	270.9	181.4
b (Å)	181.4	181.4	287.7
c (Å)	171.0	170.9	209.0
β (°)	125.3	125.3	90.0
Unique reflections	209029 (27364)	212996 (20462)	176276 (18211)
Resolution range (Å)	45.36–2.57	43.67–2.56	49.70–2.50
Completeness (%)	98.1 (95.2)	98.3 (86.1)	94.0 (88.3)
R_{int}† (%)	3.24 (12.35)	9.12 (38.43)	12.15 (51.88)
$I/\sigma(I)$	16.1 (5.5)	12.2 (2.8)	19.6 (2.9)
Redundancy	1.92 (1.8)	3.8 (3.2)	10.4 (5.7)

† $R_{int} = [(\sum_h \sum_i |F_o^2 - \langle F_o^2 \rangle|)/(\sum_h \sum_i |F_o^2|)] \times 100$ (Bruker, 2000).

CadB (*cadB*) and LdcI (*cadA*) are on the same operon (Meng & Bennett, 1992) and the induction of the *cadBA* operon is controlled by the membrane-bound regulator CadC (Tetsch *et al.*, 2007). LdcI, as observed by electron microscopy, oligomerizes to form a fivefold-symmetric decamer by the association of five dimers (Sabo *et al.*, 1974; Snider *et al.*, 2006).

In a study of potential molecular chaperones in *E. coli*, we identified a novel AAA^+ (ATPases associated with a variety of cellular activities) protein, which we termed RavA, that interacts specifically with LdcI (Snider *et al.*, 2006). RavA ATPase activity was stimulated in the presence of LdcI; however, the decarboxylation activity of LdcI was unchanged in the presence of RavA and ATP. RavA is capable of forming hexamers in the presence of ATP. The complex between RavA and LdcI was visualized by negative-stain electron microscopy and it was found that two LdcI decamers associate with up to five RavA oligomers to form a large cage-like complex (Snider *et al.*, 2006). The *in vivo* function of the RavA–LdcI interaction is uncertain. In order to obtain a better understanding of this system, we are determining the X-ray structure of LdcI.

2. Materials and methods

2.1. LdcI expression and purification

Untagged *E. coli* LdcI (Swiss-Prot entry P0A9H3) was purified as described in Snider *et al.* (2006). Briefly, BL21 (DE3) pLysS cells (Stratagene) harbouring a pET-3a plasmid (Novagen) containing the cloned LdcI gene were grown in LB medium at 310 K until mid-log phase and subsequently induced with 1 m*M* isopropyl *β*-D-1-thio-galactopyranoside (IPTG) for 4 h. Cells were harvested and frozen at 193 K. The cell pellet was resuspended in cold buffer *A* [25 m*M* Tris–HCl pH 7.5, 300 m*M* NaCl, 0.1 m*M* pyridoxal 5′-phosphate, 5%(*v*/*v*) glycerol and 1 m*M* dithiothreitol], lysed using a French press and the cellular debris was pelleted at 30 000*g* for 30 min at 277 K. The supernatant was heated in a water bath to 343 K for 5 min and subsequently spun at 30 000*g* for 15 min at 277 K. The supernatant was diluted tenfold into buffer *B* [10 m*M* HEPES pH 7.5, 0.1 m*M* pyridoxal-5′-phosphate, 5%(*v*/*v*) glycerol, 1 m*M* dithiothreitol] and loaded onto a MonoQ 5/50 GL column (General Electric). The protein was eluted using a linear 0–1000 m*M* KCl gradient in buffer *B*. LdcI fractions were concentrated using Amicon Ultra 15 centrifugal filter concentrators (Millipore) and then run through a Superdex 200 10/300 GL (GE) size-exclusion column in buffer *C* (10 m*M* HEPES pH 7.5, 300 m*M* NaCl, 0.1 m*M* pyridoxal 5′-phosphate, 1 m*M* dithiothreitol). Purified protein was concentrated to between 10 and 35 mg ml^{-1}, aliquoted into 25 ml fractions and stored at 193 K. The protein concentration was quantified using the Bradford assay (Bradford, 1976) with bovine IgG (BioShop) as a standard.

2.2. LdcI crystallization

600 µl purified untagged LdcI (10 mg ml^{-1}) was buffer-exchanged into buffer *D* [10 m*M* HEPES pH 7.5, 50 m*M* NaCl, 5%(*v*/*v*) glycerol, 0.1 m*M* pyridoxal 5′-phosphate, 1 m*M* dithiothreitol] using a PD-10 desalting column (GE), reconcentrated to 10 mg ml^{-1} using Amicon Ultra 15 centrifugal filter concentrators and submitted for high-throughput crystallization screening at the Hauptman–Woodward Institute, Buffalo, NY, USA (Luft *et al.*, 2003). From a total of 83 conditions with possible crystals, several were chosen for follow-up screening by hanging-drop vapour diffusion using 24-well Linbro plates (Hampton Research). After refinement of the initial crystallization conditions and additive screening using the Hampton Additive Screen, two different crystal forms were obtained: monoclinic *C*2 and orthorhombic $C222_1$ (Table 1). The monoclinic *C*2 crystal form

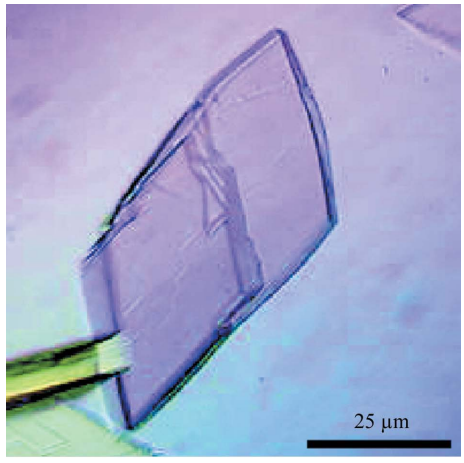

(*a*)

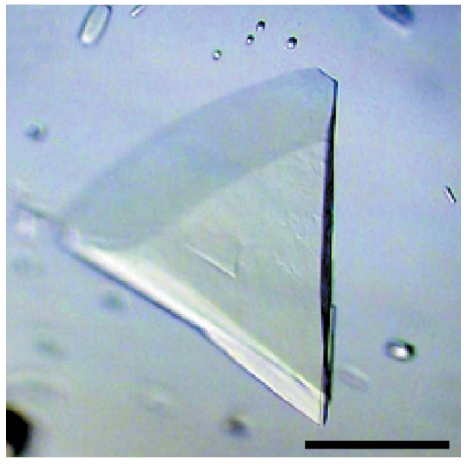

(*b*)

Figure 1
Images of representative crystals of the *C*2 (*a*) and $C222_1$ (*b*) crystal forms of LdcI. Scale bars correspond to 25 µm.

was obtained by mixing equal volumes of purified LdcI in buffer *C* (concentration range 10–35 mg ml^{-1}) with 18–28%(*w*/*v*) polyethylene glycol 1000 (PEG 1000) in buffer *E* [18–28%(*w*/*v*) PEG 1000, 100 m*M* NaCl, 100 m*M* Tris–HCl pH 8.5, 15%(*v*/*v*) glycerol, 5 m*M* tris(2-carboxyethyl)phosphine hydrochloride (TCEP)] at 285 K (Fig. 1*a*). Typically, 2 µl protein solution and 2 µl reservoir solution were mixed, spotted on a glass cover slip and placed over a greased well in a Linbro plate containing 1 ml reservoir solution. Each optimization trial used a range of PEG 1000 concentrations and the drops were left to equilibrate for one to four weeks. The higher concentrations of PEG 1000 usually produced poorly formed crystals; these crystals were used for streak-seeding into drops of lower PEG 1000 concentration, yielding well shaped crystals (unit-cell parameters a = 270.4, b = 181.4, c = 171.0 Å, β = 125.3°). Crystal-growth time varied from 10 d to several months. The addition of 3 m*M* hexammine cobalt(III) chloride to buffer *E* resulted in the orthorhombic $C222_1$ crystal form (unit-cell parameters a = 181.4, b = 287.7, c = 209.0 Å). Streak-seeding was generally not needed to grow these crystals and crystallization drops were set up with 2 µl protein solution and 2 µl mother liquor and left for one to four weeks at 285 K (Fig. 1*b*).

For derivatization of the *C*2 crystals, buffer *E* containing 26.5%(*w*/*v*) PEG 1000 was saturated with hexatantalum dodecabromide ($Ta_6Br_{12}^{2+}$) and 2 µl of this solution were mixed with drops containing crystals. The hexatantalum dodecabromide was a kind gift from Dr G. Schneider, Karolinska Institute. The progress of heavy-atom binding was easy to follow since the crystals developed a deep green colour over a period of several days.

For the collection of diffraction data, crystals were flash-frozen either in liquid nitrogen or in a cryostream attached to the diffractometer. The presence of 15%(*v*/*v*) glycerol in the crystallization condition was sufficient for cryoprotection of the crystals.

2.3. Data collection

Data sets from a native (Native-1) and a $Ta_6Br_{12}^{2+}$-derivatized (Derivative-1) *C*2 crystal were collected on the synchrotron beamline SBC-19BM-D at the Advanced Photon Source (APS), Argonne National Laboratory (ANL), Chicago, Illinois, USA and were used for phase determination (Table 1). Both data sets were collected at the wavelength corresponding to the L_{III} absorption maximum of tantalum (1.2544 Å), which was determined *via* an X-ray fluorescence spectrum recorded before the diffraction experiments. A data set from the $C222_1$ crystal form (Native-2) was collected on the synchrotron beamline BioCARS-14BM-C at the APS at a wavelength of 0.9002 Å. In general, the data were of good overall quality as assessed by the R_{int} and R_{sigma} values, but had low redundancy. The Native-1 and Derivative-1 crystals were isomorphous; derivatization with $Ta_6Br_{12}^{2+}$ did not lead to major changes to the unit-cell parameters. X-ray diffraction experiments for all crystals were performed at 100 K. All data sets were integrated and scaled using *HKL*-2000 (Otwinowski & Minor, 1997).

3. Results

3.1. Matthews coefficient and self-rotation calculations

Evidence from electron microscopy (Sabo *et al.*, 1974; Snider *et al.*, 2006) and ultracentrifugation (Sabo *et al.*, 1974) suggested that LdcI monomers associate to form dimers and decamers; five dimers are

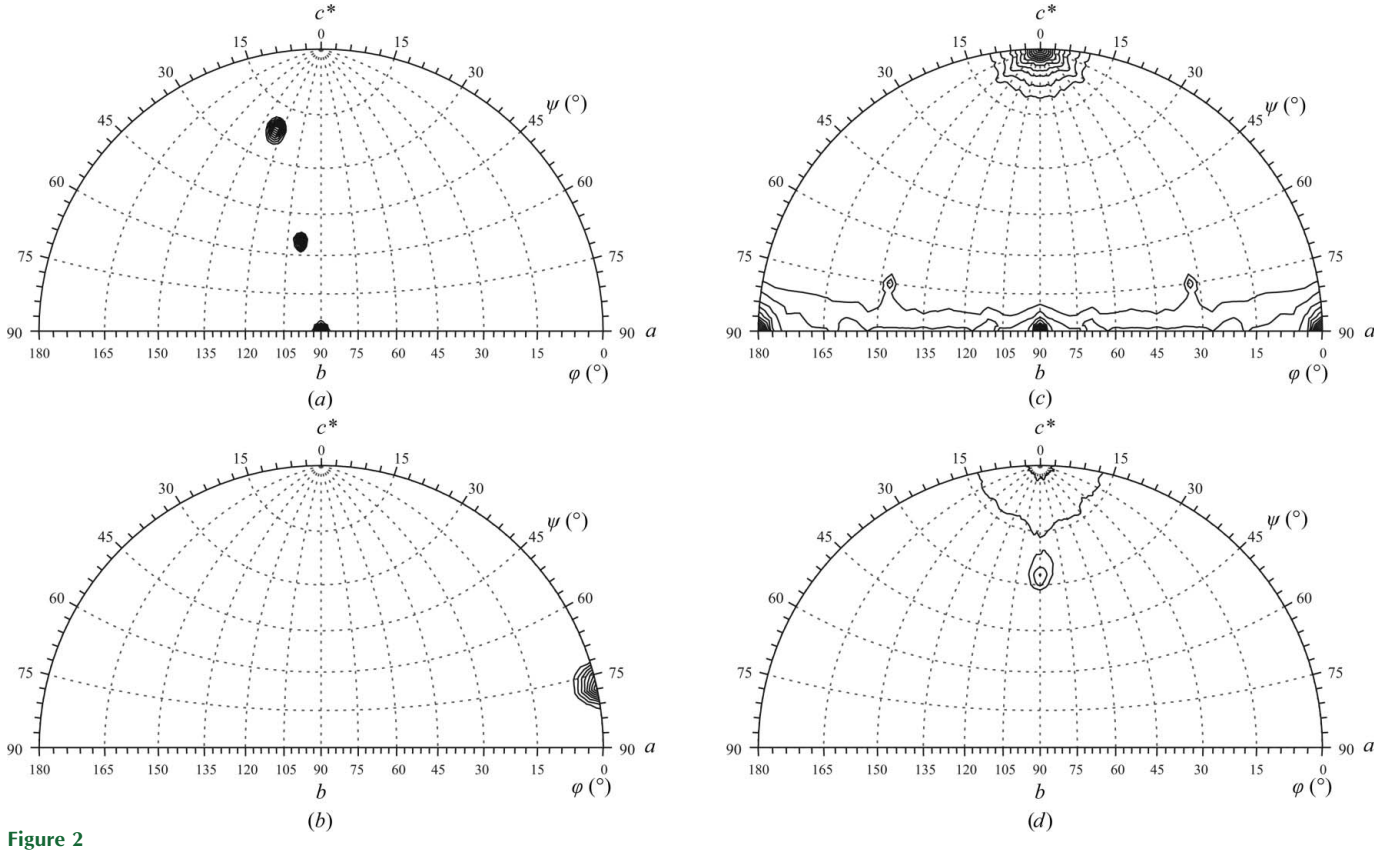

Figure 2
Self-rotation plots for (*a*) and (*b*) the *C*2 and (*c*) and (*d*) the $C222_1$ crystal forms. κ = 180° sections (*a*) and (*c*) were analyzed for twofold noncrystallographic symmetry (NCS) and κ = 72° sections (*b*) and (*d*) were analyzed for fivefold NCS. φ and ψ angles are labelled on each plot, as are the *a*, *b* and *c** axes. The images were produced using *GLRF* (Tong & Rossmann, 1997).

thought to interact to form a decamer with distinct pentameric symmetry (Snider *et al.*, 2006). In order to determine the number of monomers per asymmetric unit (ASU), the Matthews coefficient was determined and self-rotation functions were calculated for each space group using data from the Native-1 and Native-2 crystals. Matthews coefficient (Matthews, 1968; Collaborative Computational Project, Number 4, 1994) calculations indicated that between one and 12 monomers per ASU were possible for space group *C*2 and between one and ten monomers per ASU were possible for space group $C222_1$.

GLRF (Tong & Rossmann, 1997) was used to calculate self-rotation functions for both crystal forms to check for the presence of noncrystallographic symmetry (NCS; Fig. 2). The slow rotation function was evaluated in polar angles (φ, ψ, κ) with a 30 Å integration radius and data to a resolution of 3.5 Å; κ = 180° and 72° sections were examined for twofold and fivefold NCS, respectively.

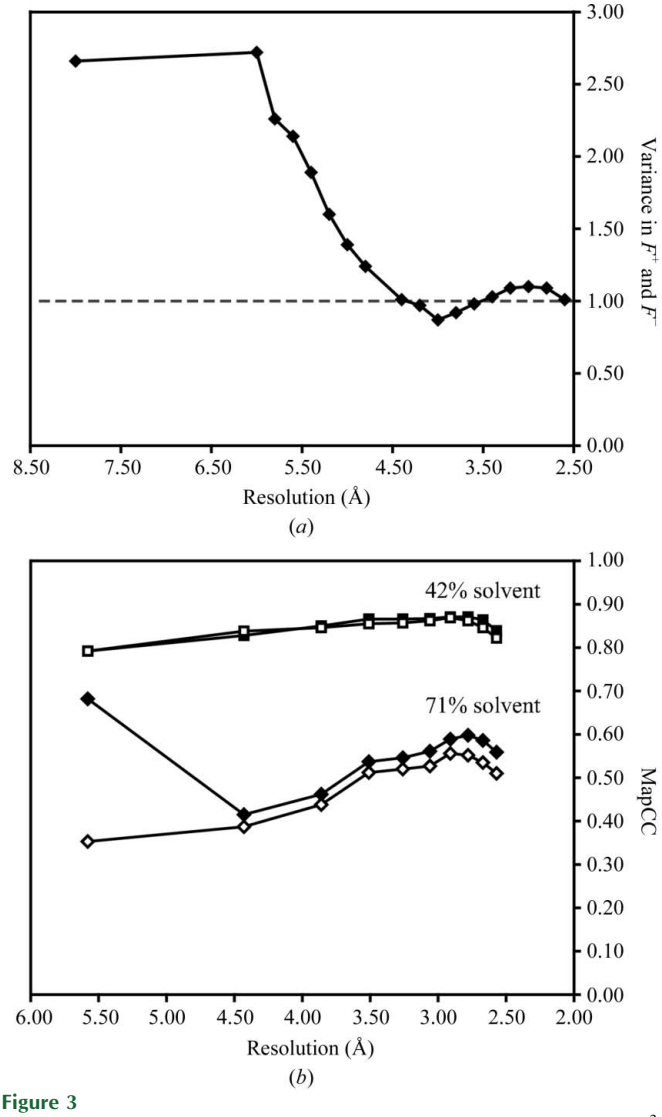

Figure 3
Analysis of the anomalous signal and determination of the hand of the $Ta_6Br_{12}^{2+}$-substructure enantiomorph. (*a*) Plot of variance in F^+ and F^- *versus* resolution. The $Ta_6Br_{12}^{2+}$ anomalous signal obtained from the Derivative-1 data set decreased rapidly beyond 5.5 Å resolution. The dashed line represents random variance in F^+ and F^-. (*b*) *SHELXE* map correlation coefficient (MapCC) *versus* resolution. Final MapCCs after 100 cycles of density modification are given for the original enantiomorph and 71% solvent content (filled diamonds), the inverted enantiomorph and 71% solvent content (diamonds), the original enantiomorph and 42% solvent content (filled squares) and the inverted enantiomorph and 42% solvent content (squares).

The rotation-function peaks were scaled to 1000 arbitrary units (AU) and contours were drawn from 400 to 1000 AU in 50 AU increments. In the κ = 180° section, the *C*2 crystal form displayed a single crystallographic twofold peak (φ = 90.00°, ψ = 90.00°) as well as two NCS twofold peaks (φ = 124.17°, ψ = 21.87° and φ = 99.17°, ψ = 55.06°). There was one NCS fivefold peak in the κ = 72° section (φ = 0°, ψ = 77.29°). The three peaks in the κ = 180° section are in a plane ψ = 12.71° from the *c** axis and each peak is separated from the next by ψ = 33–35°. The fivefold NCS peak is 90° from the plane of the twofold peaks at ψ = 12.71° from the *a* axis. The presence of the fivefold NCS peak at 90° to three twofold peaks suggests that either a pentamer with five LdcI monomers (solvent content of 71%) or a pentamer with five LdcI dimers (solvent content of 42%) is present in the asymmetric unit for the *C*2 cell. In the κ = 180° section for the $C222_1$ crystal form, only the crystallographic twofold axes were observed (φ = 0°, ψ = 0°; φ = 90°, ψ = 0°; φ = 0°, ψ = 90°); there were no strong fivefold NCS peaks in the κ = 72° section for this crystal form. Therefore, the number of monomers per ASU in the $C222_1$ crystal form could not be unambiguously determined at this stage of the analysis.

3.2. Initial phasing

The monoclinic *C*2 structure was solved first. Initial molecular-replacement trials using the noncrystallographic symmetry information derived from the self-rotation calculations and the structure of ornithine decarboxylase from *Lactobacillus* 30A (PDB code 1ord; Momany *et al.*, 1995) as a search model failed despite the 30.7% sequence identity between LdcI and the ornithine decarboxylase. An attempt to solve the structure using a selenomethionine-derivatized crystal was unsuccessful, which may be attributed to the high mosaicity of the crystals, the long *a* axis and the large number of selenium sites present in the protein (30 per monomer, which corresponds to 150 for a pentamer in the ASU or 300 for a decamer in the ASU).

The multiple isomorphous replacement approach using K_2PtCl_4, $K_2Pt(CN)_4$, $HgCl_2$ and NH_4I as sources of heavy atoms was also unsuccessful. In a successful attempt, the crystals were soaked in a $Ta_6Br_{12}^{2+}$-containing solution and a native (Native-1) as well as a derivative (Derivative-1) data set were collected at the tantalum L_{III} absorption edge (1.2544 Å; Table 1). The anomalous signal derived using *XPREP* (Bruker, 2000) was not significant for resolutions better than 5 Å (Fig. 3*a*). The positions of the $Ta_6Br_{12}^{2+}$ sites were determined by single isomorphous replacement with anomalous scattering (SIRAS) using *SHELXD* (Sheldrick, 2008) with data prepared with *XPREP* to a resolution of 5 Å. A total of 42 heavy-atom sites, representing individual $Ta_6Br_{12}^{2+}$ clusters, were identified and had correlation coefficients (CC) as defined in Schneider & Sheldrick (2002) of 37.15/25.82 [CC for all *E* values/CC for *E* values not used in substructure determination; *E* values are normalized structure factors as defined in Schneider & Sheldrick (2002); see Supplementary Table 1[1]]. Occupancy levels for the sites ranged from 5.4% to 100%. Three of the sites were on special positions along the crystallographic twofold axis; the remainder of the sites were paired across the crystallographic twofold axis. 25 of these sites conformed to the fivefold noncrystallographic symmetry predicted by the self-rotation function. Of the remaining 14 sites, nine were at probable crystal contact interfaces.

[1] Supplementary material has been deposited in the IUCr electronic archive (Reference: EN5307). Services for accessing this material are described at the back of the journal.

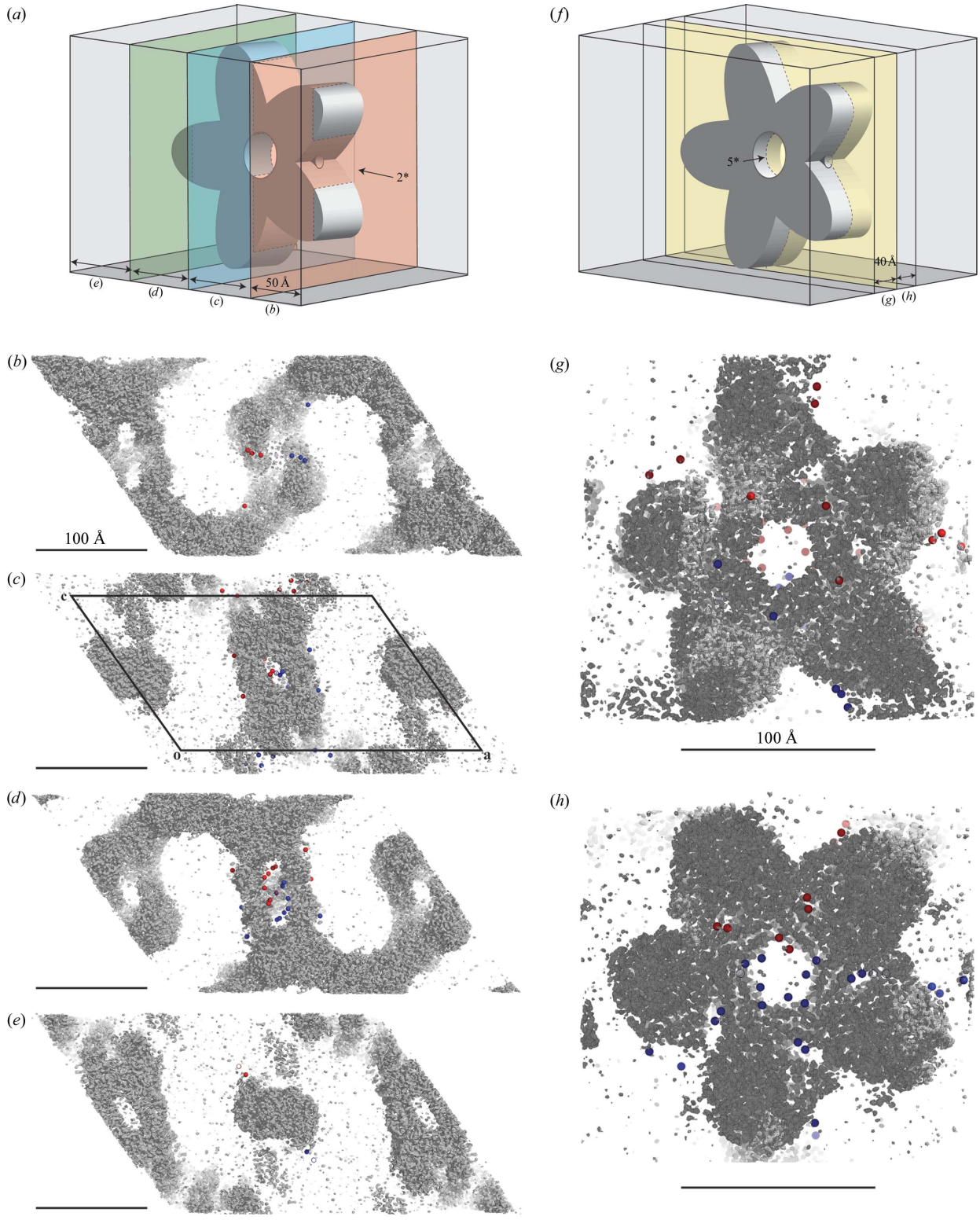

Figure 4
Sections of the *DM*-modified electron-density map contoured at 1.5σ. (*a*) shows a schematic model of the LdcI decamer based on the low-resolution negative-stain electron-microscopy reconstruction of Snider *et al.* (2006). The schematic model indicates the approximate extents of the slab sections in (*b*)–(*e*). Section (*b*) is between the front plane and the red plane. Section (*c*) is between the red and blue planes. Section (*d*) is between the blue and green planes. Section (*e*) is between the green plane and the back plane. The viewing perspective down the twofold (2*) axis is shown by the arrow in (*a*). Sections (*b*)–(*e*) represent sequential slab sections of 50 Å thickness projected down the *b* axis. Section (*c*) shows the outline of the unit cell as it appears in the sequential slabs with the origin *o* and axes *a* and *c* as indicated. The positions of $Ta_6Br_{12}^{2+}$ sites in one asymmetric unit are shown in red and the corresponding symmetry sites (about the twofold axis) are shown in blue. The schematic in (*f*) shows the slab sections in (*g*) and (*h*). Section (*g*) is between the front plane and the yellow plane. Section (*h*) is between the yellow plane and the back plane. The viewing perspective down the fivefold (5*) noncrystallographic symmetry axis (NCS) is shown by the arrow in (*f*). Sections (*g*) and (*h*) represent sequential slabs of 40 Å thickness projected down the fivefold NCS axis (12.71° from the *a* axis). Distinct fivefold symmetry is observed between many of the $Ta_6Br_{12}^{2+}$ sites. The schematic models in (*a*) and (*f*) show the position of the central pore as well as one of the side pores. Scale bars represent 100 Å.

Initial phasing and density modification were performed with *SHELXE* (Sheldrick, 2008) against Native-1 data: both substructure enantiomorphs were tested with solvent content set to either 71% (five monomers per ASU) or 42% (ten monomers per ASU) (Fig. 3*b*). Plots of the *SHELXE* map correlation coefficient (MapCC) *versus* resolution after 100 cycles of density modification were used to determine the correct substructure enantiomorph and solvent content. At a solvent content of 71%, a clear MapCC difference between the original and inverted enantiomorph was observed at low resolution (Fig. 3*b*), indicating that the original enantiomorph was correct. For the 42% solvent-content model there was no MapCC difference between the original and inverted enantiomorphs (Fig. 3*b*), so this alternative was rejected.

3.3. Density modification, averaging and phase extension

In order to improve the quality of the initial electron-density map, a further density-modification step was performed using *DM* (Cowtan, 1994). It involved 200 cycles of phase perturbation with solvent flattening at a solvent content of 71%, histogram matching, noncrystallographic symmetry averaging using the NCS operators obtained from *PROFESSS* (Collaborative Computational Project, Number 4, 1994) and phase extension from 8.00 to 2.56 Å. In the resulting electron-density map, several secondary-structure elements such as α-helices could be identified.

4. Discussion

4.1. Phasing with $Ta_6Br_{12}^{2+}$ clusters

Tantalum dodecabromide ($Ta_6Br_{12}^{2+}$) has been used in the phase determination of several different protein structures either as the only derivative, as in the case of the bacterial conjugation protein TrwB (Gomis-Rüth & Coll, 2001), or in combination with other heavy-atom derivatives, as for *Rhodobacter capsulatus* DMSO reductase (Schneider *et al.*, 1996), the *Thermoplasma acidophilum* 20S proteasome (Lowe *et al.*, 1995) and *Clostridium difficile* toxin B (Reinert *et al.*, 2005). $Ta_6Br_{12}^{2+}$ clusters consist of an octahedral arrangement of six Ta atoms bridged by 12 Br atoms along the edges of the octahedron (Supplementary Fig. 1). Six water molecules are coordinated at the vertices of the tantalum octahedron (Knablein *et al.*, 1997). $Ta_6Br_{12}^{2+}$ is useful in macromolecular structure determination for several reasons: the Ta and Br atoms have accessible anomalous scattering wavelengths (tantalum L_{III} edge at 1.25 Å; bromide *K* edge at 0.95 Å), each cluster adds a large number of electrons (856) and the deep-green colour of aqueous $Ta_6Br_{12}^{2+}$ makes derivatization of the protein sample easy to follow (Knablein *et al.*, 1997). The anomalous signal from the 4.3 Å diameter $Ta_6Br_{12}^{2+}$ clusters is very strong at resolutions lower than 5 Å, where the clusters act as single superatoms; this signal drops below 5 Å and then peaks again at about 2.7 Å before diminishing at higher resolutions (Banumathi *et al.*, 2003). For the LdcI structure, a strong anomalous signal was only observed at resolutions lower than 5 Å and the derivatized crystals did not diffract beyond 2.56 Å, limiting the ability to locate individual atoms within the cluster. However, a large number of $Ta_6Br_{12}^{2+}$-cluster sites were located in the asymmetric unit (42 sites) and this corresponds to ~8 sites per monomer. 25 of these sites (in conjunction with their symmetry mates) obeyed the fivefold noncrystallographic symmetry (NCS) and this information was used in the phase-improvement procedure. The use of $Ta_6Br_{12}^{2+}$ in solving the LdcI structure has shown the utility of this derivatization agent in cases where despite poor-quality phases, an interpretable electron-density map can be obtained and used as a starting point for molecular replacement and model refinement.

4.2. Features of the LdcI electron-density map

The *DM*-modified electron-density map (Fig. 4) shows many important features of the LdcI structure that, despite the limited quality of the phases, are in agreement with the low-resolution negative-stain electron-microscopy model of LdcI (Snider *et al.*, 2006). Observation of the map down the fivefold NCS axis reveals that portions of the electron density that correspond to an LdcI monomer obey the NCS to form a pentameric ring (Figs. 4*g* and 4*h*). Two such rings are observed stacked on top of each other with an offset of ~4° between the rings. There is a central pore down the fivefold NCS axis with a diameter of ~50 Å and 90° to this pore are five ~20 Å side pores spaced at 72° from each other (Figs. 4*b*–4*e*). Many of the $Ta_6Br_{12}^{2+}$ clusters were found to localize to either the central pore or the side pores and a number of the cluster sites that did not obey the fivefold NCS symmetry were localized to probable crystal contact interfaces. The presence of large solvent channels in the unit cell (Fig. 4*b*–4*e*) supports the 71% solvent content determined by the Matthews coefficient and the self-rotation analysis.

The data presented here represent the first step towards the determination of the atomic structure of LdcI and we anticipate that the final refined model will provide insights into the function of LdcI under acid-stress conditions, as well as the role of the RavA–LdcI interaction in *E. coli* (Snider *et al.*, 2006).

We gratefully acknowledge the generous gift of $Ta_6Br_{12}^{2+}$ from Dr G. Schneider, Karolinska Institute. We thank the following people for assistance and advice with various aspects of crystallization and structure determination: Drs S. Bryson, D. J. Lalor, J. Payandeh and B. Eger as well as A. Dong, J. P. Julien and W. Gillon. We thank the staff at the APS beamlines SBC-19-BM-D and BioCARS-14-BM-C for their time commitments and expert help. The results shown in this report are derived from work performed at Argonne National Laboratory, Structural Biology Center and BioCARS at the Advanced Photon Source. Argonne is operated by the University of Chicago Argonne LLC for the US Department of Energy, Office of Biological and Environmental Research under contract DE-AC02-06CH11357. Use of the BioCARS Sector 14 was supported by the National Institutes of Health, National Center for Research Resources under grant No. RR0077-7. UK is the recipient of a National Sciences and Engineering Research Council of Canada Postgraduate Scholarship (PGS-D), a Canadian Institutes of Health Research Strategic Training Program in the Structural Biology of Membrane Proteins Linked to Disease and a University of Toronto Open Fellowship. EA is the recipient of a fellowship from the Canadian Institutes of Health Research Strategic Training Program in Protein Folding: Principles and Diseases. This work was supported by a grant from the Canadian Institutes of Health Research (MOP-67210) to WAH as well as by the Canada Research Chairs Program and the Ontario Research and Development Challenge Fund to EFP.

References

Banumathi, S., Dauter, M. & Dauter, Z. (2003). *Acta Cryst.* D**59**, 492–498.
Boyd, R. F. (1995). *Basic Medical Microbiology*. Boston: Little, Brown & Co.
Bradford, M. M. (1976). *Anal. Biochem.* **72**, 248–254.
Bruker (2000). *SMART, SAINT, SADABS and XPREP Software Reference Manual.* Bruker AXS Inc., Madison, Wisconsin, USA.
Collaborative Computational Project, Number 4 (1994). *Acta Cryst.* D**50**, 760–763.

Cowtan, K. (1994). *Jnt CCP4/ESF–EACBM Newsl. Protein Crystallogr.* **31**, 34–38.
Foster, J. W. (1993). *J. Bacteriol.* **175**, 1981–1987.
Foster, J. W. (2004). *Nature Rev. Microbiol.* **2**, 898–907.
Gomis-Rüth, F. X. & Coll, M. (2001). *Acta Cryst.* D**57**, 800–805.
Gorden, J. & Small, P. L. (1993). *Infect. Immun.* **61**, 364–367.
Iyer, R., Williams, C. & Miller, C. (2003). *J. Bacteriol.* **185**, 6556–6561.
Kashiwagi, K., Suzuki, T., Suzuki, F., Furuchi, T., Kobayashi, H. & Igarashi, K. (1991). *J. Biol. Chem.* **266**, 20922–20927.
Knablein, J., Neuefeind, T., Schneider, F., Bergner, A., Messerschmidt, A., Lowe, J., Steipe, B. & Huber, R. (1997). *J. Mol. Biol.* **270**, 1–7.
Lee, I. S., Lin, J., Hall, H. K., Bearson, B. & Foster, J. W. (1995). *Mol. Microbiol.* **17**, 155–167.
Lowe, J., Stock, D., Jap, B., Zwickl, P., Baumeister, W. & Huber, R. (1995). *Science*, **268**, 533–539.
Luft, J. R., Collins, R. J., Fehrman, N. A., Lauricella, A. M., Veatch, C. K. & DeTitta, G. T. (2003). *J. Struct. Biol.* **142**, 170–179.
Matthews, B. W. (1968). *J. Mol. Biol.* **33**, 491–497.
Meng, S. Y. & Bennett, G. N. (1992). *J. Bacteriol.* **174**, 2659–2669.
Momany, C., Ernst, S., Ghosh, R., Chang, N. L. & Hackert, M. L. (1995). *J. Mol. Biol.* **252**, 643–655.
Otwinowski, Z. & Minor, W. (1997). *Methods Enzymol.* **276**, 307–326.
Reinert, D. J., Jank, T., Aktories, K. & Schulz, G. E. (2005). *J. Mol. Biol.* **351**, 973–981.
Richard, H. T. & Foster, J. W. (2003). *Adv. Appl. Microbiol.* **52**, 167–186.
Sabo, D. L., Boeker, E. A., Byers, B., Waron, H. & Fischer, E. H. (1974). *Biochemistry*, **13**, 662–670.
Schneider, F., Lowe, J., Huber, R., Schindelin, H., Kisker, C. & Knablein, J. (1996). *J. Mol. Biol.* **263**, 53–69.
Schneider, T. R. & Sheldrick, G. M. (2002). *Acta Cryst.* D**58**, 1772–1779.
Sheldrick, G. M. (2008). *Acta Cryst.* A**64**, 112–122.
Snider, J., Gutsche, I., Lin, M., Baby, S., Cox, B., Butland, G., Greenblatt, J., Emili, A. & Houry, W. A. (2006). *J. Biol. Chem.* **281**, 1532–1546.
Tetsch, L., Koller, C., Haneburger, I. & Jung, K. (2007). *Mol. Microbiol.* **67**, 570–583.
Texter, E. C. Jr (1968). *Am. J. Dig. Dis.* **13**, 443–454.
Texter, E. C. Jr, Chou, C. C., Laureta, H. C. & Vantrappen, G. R. (1968). *Physiology of the Gastrointestinal Tract.* St Louis, USA: C. V. Mosby Co.
Tong, L. & Rossmann, M. G. (1997). *Methods Enzymol.* **276**, 594–611.